Available online at www.CivileJournal.org

Civil Engineering Journal

(E-ISSN: 2476-3055; ISSN: 2676-6957)

Vol. 11, No. 12, December, 2025

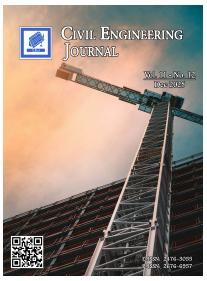

Finite Element Analysis of Concrete Beams Reinforced with Basalt Fiber-Reinforced Polymer

Poramin Sinthorn [1], Anchalee Kosittammakul [1, 2], Supakorn Tirapat [1*], Piyawat Foytong [1], Pong-in Intarit [3], Yasothorn Sapsathiarn [4], Wichairat Kaewjuea [3], Chanachai Thongchom [5], Prinya Chindaprasirt [1]

[1] *Sustainable Infrastructure Research and Development Center, Department of Civil Engineering, Faculty of Engineering, Khon Kaen University, Khon Kaen, 40002, Thailand.*

[2] *Department of Civil Engineering, Faculty of Engineering, Chulalongkorn University, Bangkok 10330, Thailand.*

[3] *Department of Civil and Environmental Engineering, Faculty of Engineering, Prince of Songkla University, Songkla 90110, Thailand.*

[4] *Department of Civil and Environmental Engineering, Faculty of Engineering, Mahidol University, Nakhon Pathom 73170, Thailand.*

[5] *Thammasat University Research Unit in Innovative Intelligent Infrastructure, Department of Civil Engineering, Thammasat School of Engineering, Thammasat University, Pathumthani 12120, Thailand.*

Received 08 August 2025; Revised 19 November 2025; Accepted 23 November 2025; Published 01 December 2025

Abstract

The increasing demand for corrosion-resistant reinforcement in concrete structures has highlighted the potential of basalt fiber-reinforced polymer (BFRP) bars as a sustainable alternative to conventional steel reinforcement. However, the flexural behavior of BFRP-reinforced concrete beams remains insufficiently characterized, particularly through advanced numerical simulation. This study develops and validates a finite element model (FEM) to analyze the flexural performance of BFRP-reinforced concrete beams and to compare it with that of steel-reinforced beams. Eight beam specimens (200 × 300 × 3,100 mm), including six reinforced with BFRP bars and two with steel bars, were modeled under four-point bending using ANSYS software. The FEM predictions were validated against experimental data and benchmarked with the design provisions of ACI 440.1R-15 and CSA S806-12. The model showed strong agreement with experimental results, yielding ultimate load ratios of 0.92–0.94 for steel-reinforced beams and 1.01–1.45 for BFRP-reinforced beams. At higher reinforcement ratios, FEM predictions tended to overestimate the capacity of BFRP-reinforced beams. While steel-reinforced beams exhibited ductile failure, BFRP-reinforced beams failed in a brittle manner. The predicted moment-deflection responses and crack patterns closely matched both experimental observations and code-based predictions. This validated FEM provides a reliable computational framework for assessing and optimizing the design of BFRP-reinforced concrete beams, thereby advancing the application of non-metallic reinforcement in structural engineering. The findings also highlight challenges in accurately modeling concrete crushing and bond behavior within FEM, indicating directions for future refinement.

Keywords: Basalt Fiber Reinforced Polymer (BFRP); Reinforced Concrete Beams; Finite Element Analysis; Flexural Behavior; Moment-Deflection Response; Crack Pattern.

1. Introduction

Structural engineering faces significant challenges in developing durable and sustainable infrastructure capable of withstanding harsh environmental conditions. Fiber-reinforced polymer (FRP) composites have emerged as an

* Corresponding author: supati@kku.ac.th

http://dx.doi.org/10.28991/CEJ-2025-011-12-09

advanced class of construction materials owing to their superior mechanical properties and durability [1, 2]. These engineered composites exhibit high strength, low self-weight, and outstanding resistance to corrosion, making them suitable for use in aggressive environments, such as those involving acid, chloride, or sulfate exposure [3-5]. FRP materials also provide high stiffness, excellent damping capacity, enhanced flexural performance, and an optimal strength-to-weight ratio [6–8].

The development of FRP technology has resulted in several variants, including glass FRP (GFRP), aramid FRP (AFRP), carbon FRP (CFRP), and basalt FRP (BFRP). Each variant possesses distinct advantages depending on the required stiffness, strength, durability, and cost considerations [8–10]. While GFRP, AFRP, and CFRP are widely adopted and covered by established design guidelines, research on BFRP remains relatively limited, rendering current knowledge insufficient to fully support its codified application in standards such as ACI 440.1R-15 [11] and CSA S806-12 [12]. Previous studies have investigated FRP for structural strengthening through externally bonded sheets, near-surface mounted (NSM) systems, and reinforcing bars, with extensive assessments under ambient, seismic, and fire conditions [1, 5, 13–17].

Among these alternatives, basalt fibers have attracted significant attention due to their distinctive combination of favorable physicochemical and mechanical properties, processability, and cost-effectiveness [18]. BFRP has demonstrated competitive performance compared to glass- and carbon-based composites, particularly in the repair and strengthening of reinforced concrete structures. Recent advances have incorporated data-driven approaches, such as acoustic emission monitoring and machine learning—including unsupervised learning techniques reported by Liu et al. [19]—to assess and monitor the performance of BFRP-strengthened beams. For instance, Feng et al. [9] investigated FRP grid reinforcement in tunnel linings, while Qiong et al. [10] proposed integrated numerical and machine learning models for FRP-reinforced columns. Moreover, additional recent studies [14, 16, 20] underscore the ongoing advancement of FRP composites in diverse structural applications. Despite these contributions, the use of BFRP rods and bars as primary reinforcement in beams continues to present challenges, particularly in terms of bond effectiveness and long-term performance.

Extensive investigations, encompassing experimental testing, theoretical analyses, and numerical modeling, have evaluated BFRP as a substitute for conventional steel reinforcement [20–22]. Reported benefits include improved mechanical performance [23–25], enhanced shear resistance [26], greater flexural strength [27], superior durability in aggressive environments [28, 29], improved deformation capacity [30], and enhanced fracture toughness [31–33]. These findings emphasize the potential of BFRP in advancing sustainable and resilient infrastructure.

The finite element method (FEM) has proven effective in simulating the behavior of FRP-reinforced structures, enabling accurate prediction of complex responses while minimizing experimental costs [34, 35]. Software platforms such as ANSYS and ABAQUS have demonstrated reliable capabilities for nonlinear modeling of FRP-reinforced systems when appropriate constitutive laws are applied [36–38]. Previous studies have validated FEM predictions against experimental outcomes, achieving close correlations with mean FEM-to-experiment ratios near unity [39, 40]. However, comprehensive validation of FEM models for BFRP-reinforced beams, particularly across varying reinforcement ratios and failure modes, remains scarce. Moreover, limitations in accurately capturing bond-slip effects and concrete crushing within FEM frameworks further justify the need for refined investigations.

The present study addresses these gaps by developing and validating a finite element model to simulate the flexural behavior of BFRP-reinforced concrete beams using ANSYS. The model is first validated against steel-reinforced specimens and subsequently extended to BFRP-reinforced beams. Numerical results are benchmarked against the experimental work of Elgabbas et al. [24] and evaluated against ACI 440.1R-15 [11] and CSA S806-12 [12]. Crack patterns, moment–deflection relationships, and ultimate capacities are analyzed to provide new insights into the structural behavior of BFRP reinforcement and its implications for practical design.

The remainder of this paper is organized as follows: Section 2 describes the materials, reinforcement details, and finite element modeling procedure. Section 3 presents the results of the FEM analysis, including validation against experimental data and design codes, and discusses the implications of the findings. Finally, Section 4 provides the main conclusions and recommendations for future research.

2. Materials and Methods

To provide an overview of the methodology, the overall research process is summarized in a flowchart as demonstrated in Figure 1. The procedure begins with the identification of the problem statement and the collection of experimental data for benchmark specimens. Subsequently, a finite element model was developed in ANSYS, validated against two steel-reinforced beams, and extended to six BFRP-reinforced specimens with different reinforcement ratios and bar diameters. Comparative analyses were performed between FEM predictions, experimental data from Elgabbas et al. [24], and code-based calculations according to ACI 440.1R-15 [11] and CSA S806-12 [12]. Finally, the results were synthesized and discussed to derive structural insights and practical implications for design.

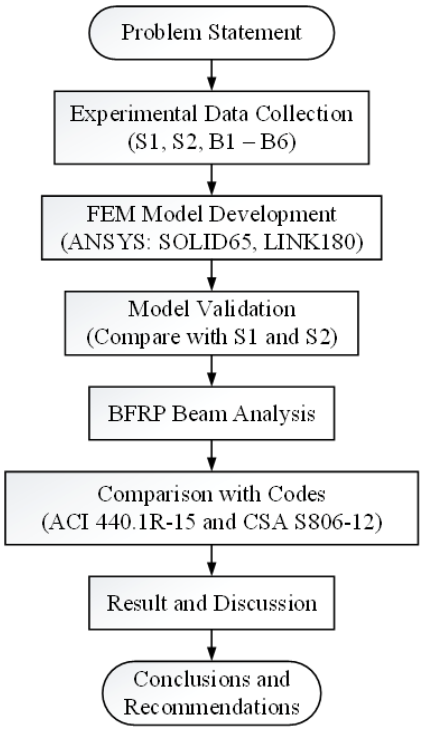

Figure 1. Flowchart illustrating the scope of the study

Following the methodological framework presented in Figure 1, this section is organized into three main parts. Section 2.1 describes the mechanical properties of the materials used in the specimens, including BFRP and steel reinforcement bars. Section 2.2 outlines the reinforcement details, such as reinforcement ratios and the design assumptions adopted from ACI 440.1R-15 and CSA S806-12. Section 2.3 presents the finite element modeling approach in ANSYS, including the adopted element types, constitutive material models, boundary conditions, and validation strategy. Together, these subsections establish the basis for the numerical analysis and comparisons discussed in the subsequent sections.

2.1. Materials Properties

The mechanical properties of the reinforcement bars used in this study are summarized in Table 1. The reinforcement consisted of basalt fiber-reinforced polymer (BFRP) bars with diameters of 8, 12, and 16 mm, and steel bars with diameters of 10 and 15 mm. The key properties considered include cross-sectional area, elastic modulus (E), ultimate tensile strength of BFRP (f_{fu}), yield strength of steel (f_y), and the corresponding ultimate strain of BFRP (ε_{fu}) and yield strain of steel (ε_y). In this notation, the subscript f refers to BFRP bars, while the subscript s denotes steel reinforcement.

Table 1. Properties of materials [24]

Materials	Diameter (mm)	Cross section area (mm²)	Elastic modulus, E (GPa)	f_{fu} (MPa)	f_y (MPa)	$\varepsilon_{fu} = \frac{f_{fu}}{E_f}$	$\varepsilon_y = \frac{f_y}{E_s}$
BFRP	8	50	64.6	1655	-	0.0256	-
BFRP	12	113	69.3	1760	-	0.0254	-
BFRP	16	201	64.8	1724	-	0.0266	-
Steel	10	100	200	-	450	-	0.0023
Steel	15	200	200	-	450	-	0.0023

2.2. Reinforcement Details

Table 2 presents various reinforcement configurations, including reinforcement ratios and concrete strength parameters. The specimens were designed with different reinforcement ratios (ρ_f) to evaluate their influence on beam behavior. Using specified compressive strength of concrete (f_c'), balanced reinforcement ratios (ρ_{fb}) were calculated according to ACI 440.1R-15 [11] and CSA S806-12 [12] using Equations 1 and 3. The stress block parameters (α_1 and β_1) were determined using Equations 2 and 4 for ACI 440.1R-15 and CSA S806-12 codes, respectively. Analysis of reinforcement ratios ($\frac{\rho_f}{\rho_{fb}}$) showed ranges of 1.52-6.81 for ACI 440.1R-15 and 1.81-8.17 for CSA S806-12, with variations attributed to different assumptions in stress-strain behavior and internal force distributions. BFRP-reinforced

beams were designed to fail by concrete crushing at maximum compressive strains (ε_{cu}) of 0.003 for ACI 440.1R-15 and 0.0035 for CSA S806-12, while steel-reinforced control beams were designed as under-reinforced sections to ensure yielding behavior. For ACI 440.1R-15 [11]:

$$\rho_{fb} = \alpha_1 \beta_1 \frac{f_c^{'}}{f_{fu}} \frac{E_f \varepsilon_{cu}}{E_f \varepsilon_{cu} + f_{fu}} \quad (1)$$

$$\text{where; } \alpha_1 = 0.85 \text{ and } \beta_1 = 0.85 - 0.05\left(\frac{f_c^{'} - 28}{7}\right) \quad (2)$$

and CSA S806-12 [12]:

$$\rho_{fb} = \alpha_1 \beta_1 \frac{0.65 f_c^{'}}{f_{fu}} \frac{\varepsilon_{cu}}{\varepsilon_{cu} + \varepsilon_{fu}} \quad (3)$$

$$\text{where; } \alpha_1 = 0.85 - 0.0015 f_c^{'} \geq 0.67 \text{ and } \beta_1 = 0.97 - 0.0025 f_c^{'} \geq 0.67 \quad (4)$$

Table 2. Details of reinforcement

Specimen	Reinforcement detail	Effective depth (mm)	f'_c (MPa)	ρ_s	ρ_f	ρ_s/ρ_{sb}		ρ_f/ρ_{fb}	
						ACI 440.1R-15 [11]	CSA S806-12 [12]	ACI 440.1R-15 [11]	CSA S806-12 [12]
S1	2-D10	257	44.7	0.0039	-	0.11	0.09	-	-
S2	2-D15	254		0.0079	-	0.22	0.18	-	-
B1	3-8 mm	258	52.7	-	0.0029	-	-	1.52	1.81
B2	5-8 mm	244		-	0.0051	-	-	2.68	3.19
B3	2-12 mm	256	44.7	-	0.0044	-	-	2.65	3.29
B4	3-12 mm	256		-	0.0066	-	-	3.97	4.93
B5	2-16 mm	254	50.8	-	0.0079	-	-	4.54	5.45
B6	3-16 mm	254		-	0.0119	-	-	6.81	8.17

2.3. Finite Element Model

2.3.1. Geometric Modelling

Eight beam specimens were analyzed using ANSYS finite element software. The beams were modeled with dimensions of 200 mm × 300 mm × 3,100 mm and calibrated against experimental data from Elgabbas et al. [24]. The analysis included six BFRP-reinforced beams with bar diameters of 8, 12, and 16 mm, and two steel-reinforced reference beams with bar diameters of 10 and 15 mm. All specimens featured compression reinforcement consisting of two 10-mm diameter bars (2-D10) and stirrups of 10-mm diameter at 100-mm spacing (1-D10@100), with varied stirrup spacing in the moment zone to examine flexural behavior effects. The beams were analyzed under four-point bending conditions using displacement-controlled loading. Figure 2 and Table 2 present the reinforcement details and material properties, while Figure 3 illustrates the test configuration.

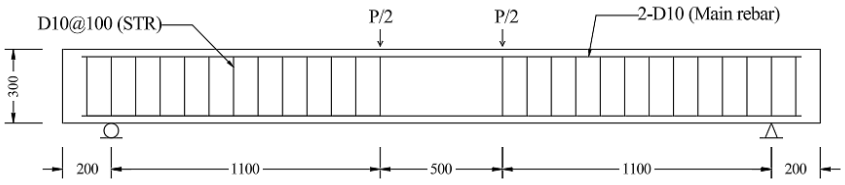

Figure 2. Beam geometry and reinforcement details (dimensions in millimeters)

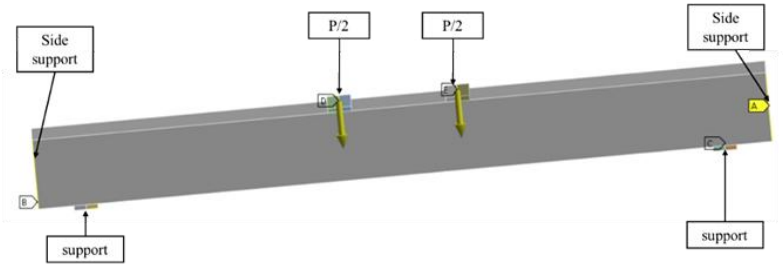

Figure 3. Four-point bending test configuration in ANSYS

2.3.2. Element Type and Model

The finite element model utilized SOLID65 elements for concrete and LINK180 elements for reinforcement. The concrete material behavior was simulated using the Willam & Warnke [41] nonlinear constitutive model. This model accounts for concrete cracking under tension and crushing under compression, along with the development of reinforcement plasticity [42]. The nonlinear response is characterized by multi-linear stress-strain relationships as depicted in Figure 4-a. For the compressive behavior of concrete, the stress-strain relationship follows the model proposed by Hognestad et al. [43], which is governed by the following Equations

$$f_c = f_c'' \left[\frac{2\varepsilon_c}{\varepsilon_{c0}} - \left(\frac{\varepsilon_c}{\varepsilon_{c0}}\right)^2\right] \text{ where } 0 \le \varepsilon_c \le \varepsilon_{c0} \quad (5)$$

$$f_c = f_c'' - \left(\frac{0.15 f_c''}{0.0038 - \varepsilon_{c0}}\right)(\varepsilon_c - \varepsilon_{c0}) \text{ where } \varepsilon_c > \varepsilon_{c0} \quad (6)$$

$$\varepsilon_{c0} = \frac{2 f_c''}{E_c} \text{ where } f_c'' = 0.9 f_c' \text{ and } E_c = 4730\sqrt{f_c'} \quad (7)$$

where f_c is the concrete compressive strength (MPa) corresponding to the strain value ε_c, f_c'' is the reduced compressive strength of concrete (MPa), and E_c is the modulus of elasticity of concrete (MPa).

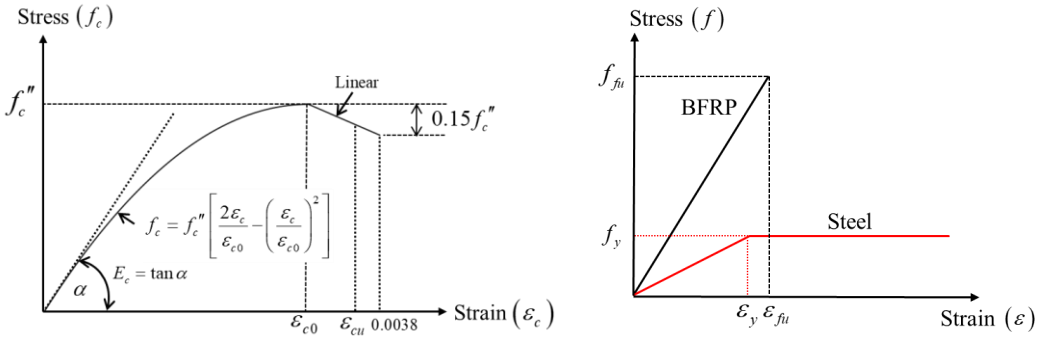

Figure 4. Material constitutive models used in FEM analysis: **(a) nonlinear stress-strain relationship for concrete, and (b) linear elastic and bilinear behavior for BFRP and steel reinforcement**

Concrete elements were modeled using eight-node SOLID65 elements with three translational degrees of freedom per node in x, y, and z directions, enabling simulation of plastic deformation, three-directional cracking, and crushing. LINK180 elements were used to model both BFRP and steel reinforcement, providing three degrees of freedom per node with capabilities for plasticity, creep, and large deformation analysis. The material models, shown in Figure 4-b, followed bilinear constitutive behavior for steel and linear elastic behavior until rupture for BFRP. The finite element model consisted of 12,500 elements, comprising 12,000 concrete elements and 500 reinforcement elements, as illustrated in Figure 5.

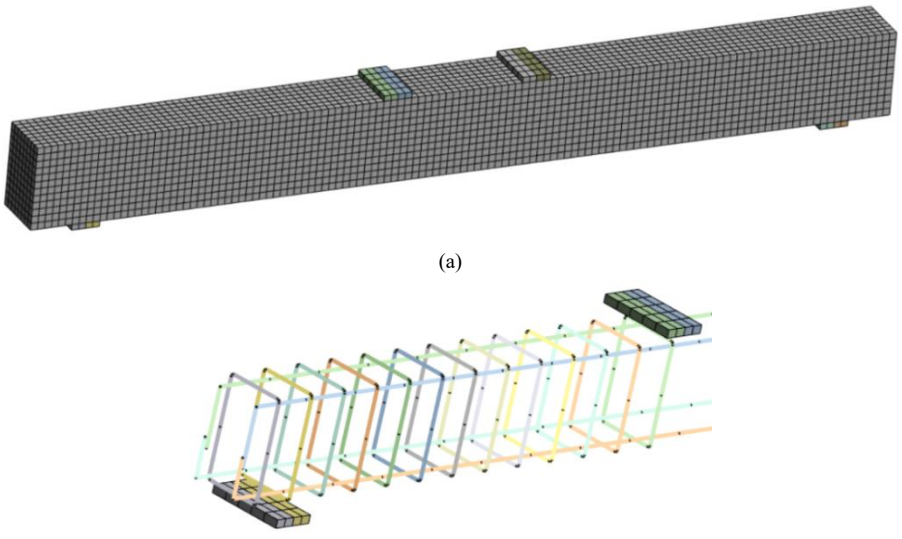

Figure 5. Finite element mesh discretization: **(a) concrete elements, and (b) reinforcement elements**

3. Results and Discussion

This section presents the results of the finite element analysis (FEA) of BFRP- and steel-reinforced concrete beams, together with a comprehensive discussion of their structural behavior. The analysis is structured to first validate the FEM predictions against experimental data reported by Elgabbas et al. [24]. Subsequent subsections examine ultimate moment capacity (M_n), moment–deflection behavior, and crack pattern development, followed by a comparison with design code provisions (ACI 440.1R-15 [11] and CSA S806-12 [12]). The discussion highlights both the accuracy and limitations of FEM in capturing the structural response, as well as the implications for practical design.

3.1. Validation of Finite Element Method

The validation process was carried out by comparing the ultimate moment capacities predicted by the finite element model ($M_{n\ FEM}$) with the experimental results ($M_{n\ Exp}$) reported by Elgabbas et al. [24]. For conventional reinforced concrete (RC) beams S1 and S2, the capacity ratios ($M_{n\ FEM}/M_{n\ Exp}$) were 0.92 and 0.94, respectively, indicating strong agreement. As shown in Table 3, beam S1 exhibited an experimental ultimate moment of 31.33 kN·m, compared with 28.85 kN·m from FEM, while the ACI and CSA predictions were lower at 22.60 kN·m and 22.24 kN·m, respectively. Similarly, beam S2 recorded an experimental value of 51.60 kN·m, compared with 48.29 kN·m from FEM, while ACI and CSA predicted 43.59 kN·m and 42.16 kN·m, respectively. The moment–deflection relationships in Figure 6 confirm that FEM captured the yield point and ductile response characteristic of steel reinforcement with high accuracy.

Table 3. Ultimate moment of steel-BFRP reinforced beams

Specimen	Ultimate moment, M_n (kN-m)				$\frac{M_{n\ FEM}}{M_{n\ EXP}}$	$\frac{M_{n\ ACI}}{M_{n\ EXP}}$	$\frac{M_{n\ CSA}}{M_{n\ EXP}}$
	$M_{n\ EXP}$	$M_{n\ FEM}$	$M_{n\ ACI}$	$M_{n\ CSA}$			
S1	31.33	28.85	22.60	22.24	0.92	0.72	0.71
S2	51.60	48.29	43.59	42.16	0.94	0.84	0.82
B1	52.85	53.20	49.06	43.51	1.01	0.93	0.82
B2	65.45	80.08	56.21	49.19	1.22	0.86	0.75
B3	54.40	58.26	56.75	48.55	1.07	1.04	0.89
B4	67.02	97.16	67.23	56.83	1.45	1.00	0.85
B5	71.09	90.71	72.38	62.16	1.28	1.02	0.87
B6	91.03	110.51	85.17	72.11	1.21	0.94	0.79

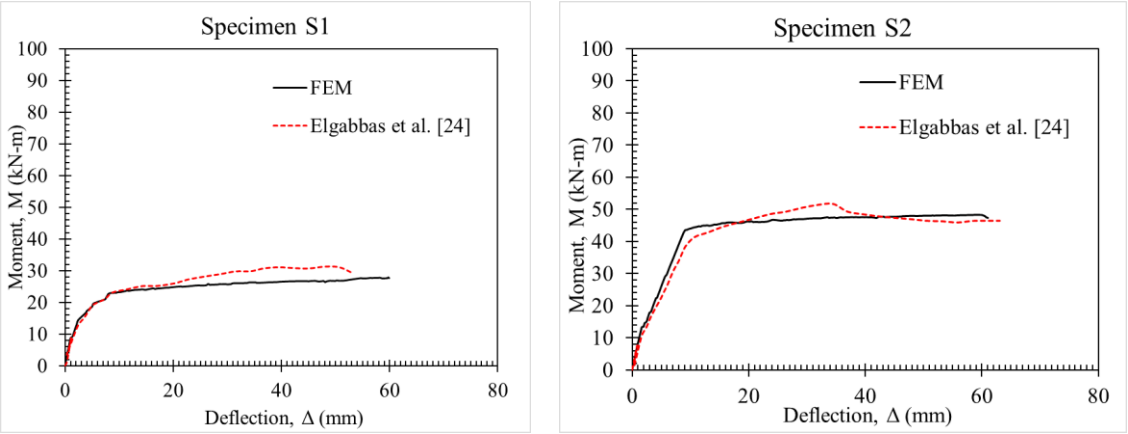

Figure 6. Comparison between FEM and experiment for steel reinforcement

For BFRP-reinforced beams, the ratios $M_{n\ FEM}/M_{n\ Exp}$ ranged from 1.01 to 1.45, reflecting variable levels of prediction accuracy. Beam B1 demonstrated the closest agreement ($M_{n\ FEM}/M_{n\ Exp}$ = 1.01), with FEM predicting 53.20 kN·m compared with the experimental value of 52.85 kN·m. Beam B3 exhibited a ratio of 1.07, while beams B2, B5, and B6 showed overestimations ranging between 1.21 and 1.28. The largest discrepancy occurred in beam B4, where FEM predicted 97.16 kN·m compared with an experimental value of 67.02 kN·m, yielding a ratio of 1.45. These trends are consistent with previous reports by Vacev et al. [44] and Mohyeddin et al. [45], who noted that FEM frequently overestimates load-carrying capacity relative to both experiments and code-based estimates.

The tendency of FEM to overestimate capacity can be attributed to several factors, including the assumption of a perfect bond between BFRP and surrounding concrete–which neglects bond–slip effects [46], the lack of tension-stiffening representation in the adopted concrete model, and the inherently brittle response of BFRP reinforcement at

higher reinforcement ratios. As emphasized by Ovitigala et al. [30] and Abushanab et al. [35], accurate representation of bond–slip behavior and crack development is essential for predicting the performance of BFRP beams. Therefore, while FEM provides reliable predictions for steel-reinforced beams and BFRP beams with lower reinforcement ratios, its accuracy declines in heavily reinforced BFRP specimens.

3.2. Ultimate Flexural Strength

The evaluation of ultimate flexural strength is essential to verify the accuracy of FEM predictions and to assess the reliability of design provisions. This subsection compares the ultimate moment capacities obtained from experiments, FEM simulations, and analytical calculations based on ACI 440.1R-15 [11] and CSA S806-12 [12]. The comparison highlights the effectiveness of FEM in capturing flexural behavior and provides insight into the conservatism of current design codes. The design methodology for FRP-reinforced concrete sections governs the moment capacity through concrete crushing failure, which occurs at maximum compressive strains (ε_{cu}) of 0.003 for ACI 440.1R-15 and 0.0035 for CSA S806-12. This approach ensures that failure occurs before the BFRP bars reach their ultimate tensile capacity in over-reinforced sections. The ultimate moment capacity analysis, summarized in Table 3 and calculated using Equations 8 to 13, demonstrates consistent trends across experimental results, FEM predictions, and design code provisions.

$$M_n = A_f f_f \left(d - \frac{a}{2}\right) \tag{8}$$

$$f_f = E_f \varepsilon_{cu} \left(\frac{\beta_1 d - a}{a}\right) \text{ when } f_f \le f_{fu} \tag{9}$$

and;

$$a = \frac{A_f f_f}{\alpha_1 f_c' b} \text{ for ACI440.1R-15} \tag{10}$$

$$f_f = \sqrt{\frac{(E_f \varepsilon_{cu})^2}{4} + \frac{\alpha_1 \beta_1 f_c'}{\rho_f} E_f \varepsilon_{cu}} - \frac{E_f \varepsilon_{cu}}{2} \text{ for ACI440.1R-15} \tag{11}$$

$$a = \frac{A_f f_f}{0.65 \alpha_1 f_c' b} \text{ for CSA S806-12} \tag{12}$$

$$f_f = \sqrt{\frac{(E_f \varepsilon_{cu})^2}{4} + \frac{0.65 \alpha_1 \beta_1 f_c'}{\rho_f} E_f \varepsilon_{cu}} - \frac{E_f \varepsilon_{cu}}{2} \text{ for CSA S806-12} \tag{13}$$

where, M_n is the nominal moment capacity (N·mm); A_f is the area of fiber-reinforced polymer (FRP) reinforcement (mm^2); f_f is stress in FRP reinforcement in tension (MPa); d is the distance from extreme compression fiber to centroid of tension reinforcement (mm); a is the depth of equivalent rectangular stress block (mm); and b is the width of rectangular cross section (mm).

For the steel-reinforced control beams, specimen S1 exhibited an experimental ultimate moment of 31.33 kN·m, with prediction ratios of 0.92, 0.72, and 0.71 for FEM, ACI, and CSA, respectively. Similarly, specimen S2 reached an experimental value of 51.60 kN·m, with corresponding prediction ratios of 0.94, 0.84, and 0.82. These results confirm that FEM provides accurate predictions for steel reinforcement, while the code-based methods remain conservative.

For beams reinforced with BFRP, the performance varied with reinforcement ratio. In the lower reinforcement group, B1 achieved an experimental ultimate moment of 52.85 kN·m, with prediction ratios of 1.01, 0.93, and 0.82 for FEM, ACI, and CSA, respectively. B2 recorded a higher experimental value of 65.45 kN·m, with ratios of 1.22, 0.86, and 0.75. In the medium reinforcement group, B3 reached 54.40 kN·m with ratios of 1.07, 1.04, and 0.89, while B4 achieved 67.02 kN·m, but FEM significantly overpredicted its capacity, yielding a ratio of 1.45 compared to 1.00 for ACI and 0.85 for CSA. For beams with higher reinforcement ratios, B5 exhibited an experimental capacity of 71.09 kN·m with prediction ratios of 1.28, 1.02, and 0.87, and B6 reached the highest experimental capacity of 91.03 kN·m with corresponding ratios of 1.21, 0.94, and 0.79.

Overall, FEM predictions tended to overestimate the moment capacity of BFRP-reinforced beams, with ratios ranging from 1.01 to 1.45. By contrast, ACI 440.1R-15 exhibited closer agreement with experimental results, with ratios between 0.86 and 1.04, while CSA S806-12 consistently underestimated the capacity with ratios of 0.75 to 0.89. The observed increase in ultimate moment capacity with higher reinforcement ratios is consistent with the findings of Ovitigala et al. [30], confirming that flexural strength in BFRP-reinforced beams is strongly influenced by reinforcement ratio.

Notably, both ACI and CSA predictions were consistently lower than experimental and FEM results, highlighting the conservative nature of these design provisions. This conservative estimation is beneficial in practice, as it ensures a

safety margin when applying FRP materials in structural design [47]. However, the tendency of FEM to overestimate capacities—particularly at higher reinforcement ratios—underscores the need for refined constitutive models that incorporate bond–slip behavior and tension-stiffening effects.

3.3. Moment-Deflection Behavior

The relationship between applied bending moment and mid-span deflection is a fundamental indicator of flexural performance in reinforced concrete beams. It provides direct insight into stiffness degradation, crack initiation and propagation, and overall ductility. Evaluating this relationship is therefore essential for assessing both serviceability and ultimate limit states. In the present study, moment–deflection behavior was investigated for BFRP-reinforced beams using FEM simulations, experimental results reported by Elgabbas et al. [24], and analytical predictions derived from ACI 440.1R-15 [11] and CSA S806-12 [12].

The moment–deflection response can be divided into two distinct stages. In the initial uncracked stage, behavior is governed by the gross moment of inertia (Ig), with deflection determined directly from the applied moment (M_a). Once the applied moment exceeds the cracking moment (M_{cr}), the beam enters the cracked stage, where stiffness is governed by the cracked moment of inertia (I_{cr}). The cracking moment, M_{cr}, marks the onset of flexural cracking and is a key indicator of the serviceability limit state. It can be calculated using the modulus of rupture, f_r, as shown in Equation 14. The modulus of rupture is further defined according to ACI 440.1R-15 [11] and CSA S806-12 [12] in Equations 15 and 16, respectively.

$$M_{cr} = \frac{f_r I_g}{y_t} \tag{14}$$

$$f_r = 0.62\sqrt{f_c'} \quad \text{for} \quad \text{ACI440.1R-15} \tag{15}$$

$$f_r = 0.60\sqrt{f_c'} \quad \text{for} \quad \text{CSAS806-12} \tag{16}$$

where y_t is the distance from the centroidal axis of gross section, neglecting reinforcement, to tension face (mm), and f_r is the modulus of rupture of concrete (MPa), determined according to Equations 15 and 16 for the ACI 440.1R-15 and CSA S806-12 provisions, respectively.

Following cracking, deflection behavior is better represented using the concept of effective moment of inertia, I_e, which accounts for the progressive reduction in stiffness due to crack propagation. The ACI 440.1R-15 provisions define I_e through a set of empirical Equations 17 to 21, while CSA S806-12 provides a simplified expression given in Equation 22. In these formulations, l denotes the distance from the support to the loading point, L represents the clear span length between supports, and n_f is the modular ratio, defined as the ratio of the modulus of elasticity of BFRP bars to that of concrete. These equations allow calculation of deflections for simply supported beams subjected to two-point loading, as in the present study.

For ACI 440.1R-15:

$$\Delta = \frac{Pl}{24E_cI_e}(3L^2 - 4l^2) \tag{17}$$

$$I_e = \frac{I_{cr}}{1-\gamma\left(\frac{M_{cr}}{M_a}\right)^2\left[1-\frac{I_{cr}}{I_g}\right]} \leq I_g \text{ when } M_a \geq M_{cr} \tag{18}$$

$$\gamma = 1.72 - 0.72\left(\frac{M_{cr}}{M_a}\right) \tag{19}$$

$$I_{cr} = \frac{bd^3}{3}k^3 + n_f A_f d^2(1-k)^2 \tag{20}$$

$$k = \sqrt{2\rho_f n_f + (\rho_f n_f)^2} - \rho_f n_f \tag{21}$$

For CSA S806-12:

$$\Delta = \frac{Pl}{24E_cI_{cr}}(3L^2 - 4l^2 - 8\eta l^2) \text{ and } \eta = \left(1 - \frac{I_{cr}}{I_g}\right) \tag{22}$$

Figure 7 illustrates the moment–deflection curves. For beams with lower reinforcement ratios (B1–B3), FEM predictions showed strong agreement with experimental results up to deflections of approximately 40 mm, validating the applicability of the effective moment of inertia concept at moderate load levels. In contrast, beams with higher reinforcement ratios (B4–B6) demonstrated larger discrepancies beyond this range. Specimen B4 showed the greatest divergence, with FEM overestimating the ultimate moment by approximately 35%. Beams B5 and B6 initially showed close agreement with experiments in the serviceability range; however, FEM consistently overpredicted ultimate capacity by about 10% at larger deflections.

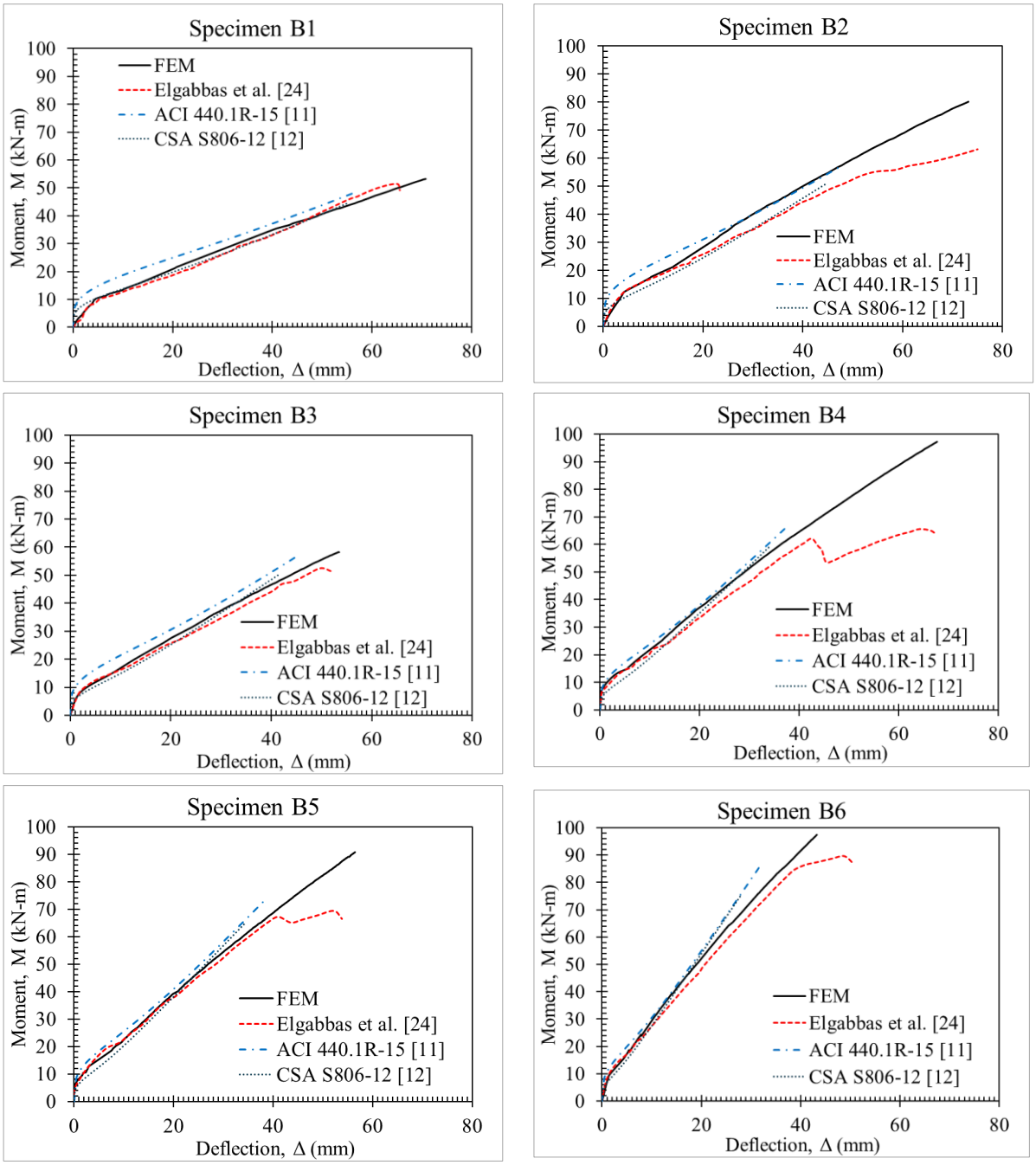

Figure 7. Moment-deflection response of BFRP-reinforced beams

These discrepancies highlight the limitations of FEM in modeling nonlinear mechanisms such as bond degradation, loss of tension stiffening, and crack localization at advanced loading stages. While ACI and CSA design codes provide conservative moment–deflection predictions, FEM offers more accurate representation of intermediate-stage behavior but tends to overestimate capacities in heavily reinforced beams. These findings are consistent with observations by Ovitigala et al. [30] and Abushanab et al. [35], who emphasized the influence of reinforcement ratio and bond–slip effects on flexural behavior. Overall, the results confirm that moment–deflection behavior is directly governed by effective stiffness reduction mechanisms, as expressed in Equation 17 to 22, with reinforcement ratio serving as a critical parameter influencing both serviceability and ultimate response.

3.4. Effect of Reinforcement Ratio

The reinforcement ratio is a key parameter governing the flexural performance of reinforced concrete beams, influencing stiffness, ductility, and failure mode. To investigate this effect, normalized moment–deflection curves were compared for all tested specimens, as shown in Figure 8. The BFRP-reinforced beams (B1–B6) exhibited progressively steeper slopes with increasing reinforcement ratios, reflecting enhanced sectional stiffness and reduced deformability. In contrast, the steel-reinforced specimens (S1–S2), highlighted in red, displayed distinctive yielding plateaus associated

with the plastic behavior of steel reinforcement, which differs fundamentally from the predominantly linear elastic response observed in BFRP-reinforced specimens.

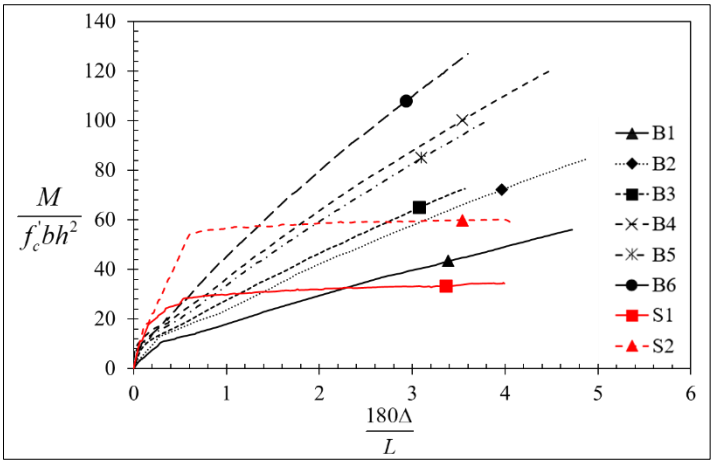

Figure 8. Response of normalized moment versus normalized deflection for BFRP and steel-reinforced beams

The relationship between normalized moment capacity and reinforcement ratio ($\frac{\rho_f}{\rho_{fb}}$) was further examined through power-function curve fitting analysis, as illustrated in Figure 9. The finite element predictions closely followed experimental trends, yielding coefficients of determination (R^2) of 0.8657 for ACI 440.1R-15 and 0.7346 for CSA S806-12 approaches. Experimental results demonstrated even stronger correlations, with R^2 values of 0.9608 for CSA and 0.8935 for ACI predictions. These correlations covered reinforcement ratios ranging from 1.18 to 5.14 for CSA and 1.54 to 6.87 for ACI provisions. Notably, the experimental–CSA correlation achieved superior predictive accuracy (R^2 = 0.9608) compared to the experimental–ACI correlation (R^2 = 0.8935).

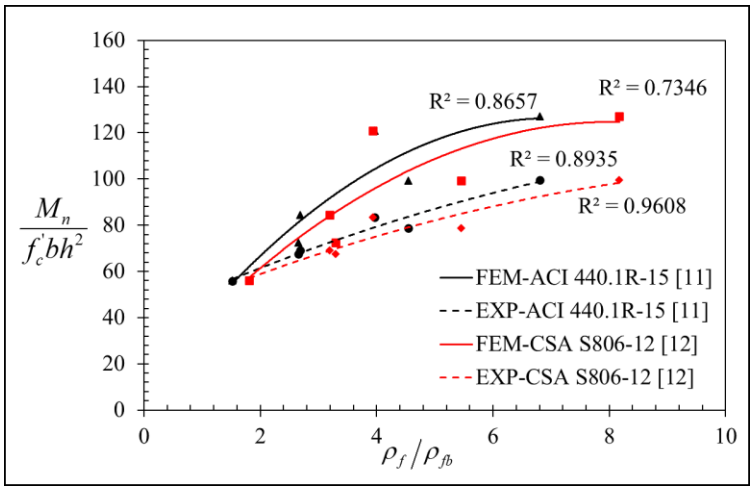

Figure 9. Effect of reinforcement ratio ($\frac{\rho_f}{\rho_{fb}}$) on normalized ultimate moment: comparison of FEM and experimental results with design code predictions

Overall, the results confirm that the flexural strength of BFRP-reinforced beams increases with reinforcement ratio, but at the expense of ductility, as reflected in the nearly linear moment–deflection response. These findings are consistent with those reported by Elgabbas et al. [24] and Ovitigala et al. [30], who emphasized the strong influence of reinforcement ratio on both strength and deformation characteristics. The superior correlation observed with CSA-based predictions further highlights the conservatism of ACI provisions relative to experimental data.

3.5. Crack Pattern Prediction

Accurate prediction of crack formation and propagation is a critical measure of the validity of finite element models, as it reflects the capability of the numerical approach to capture bond behavior, stress redistribution, and ultimate failure mechanisms. In this study, experimental crack patterns reported by Elgabbas et al. [24] were compared with FEM predictions for both steel- and BFRP-reinforced beams, as illustrated in Figure 10. Overall, the FEM results demonstrated close agreement with experimental observations, successfully reproducing the initiation and progression of cracks under increasing loads.

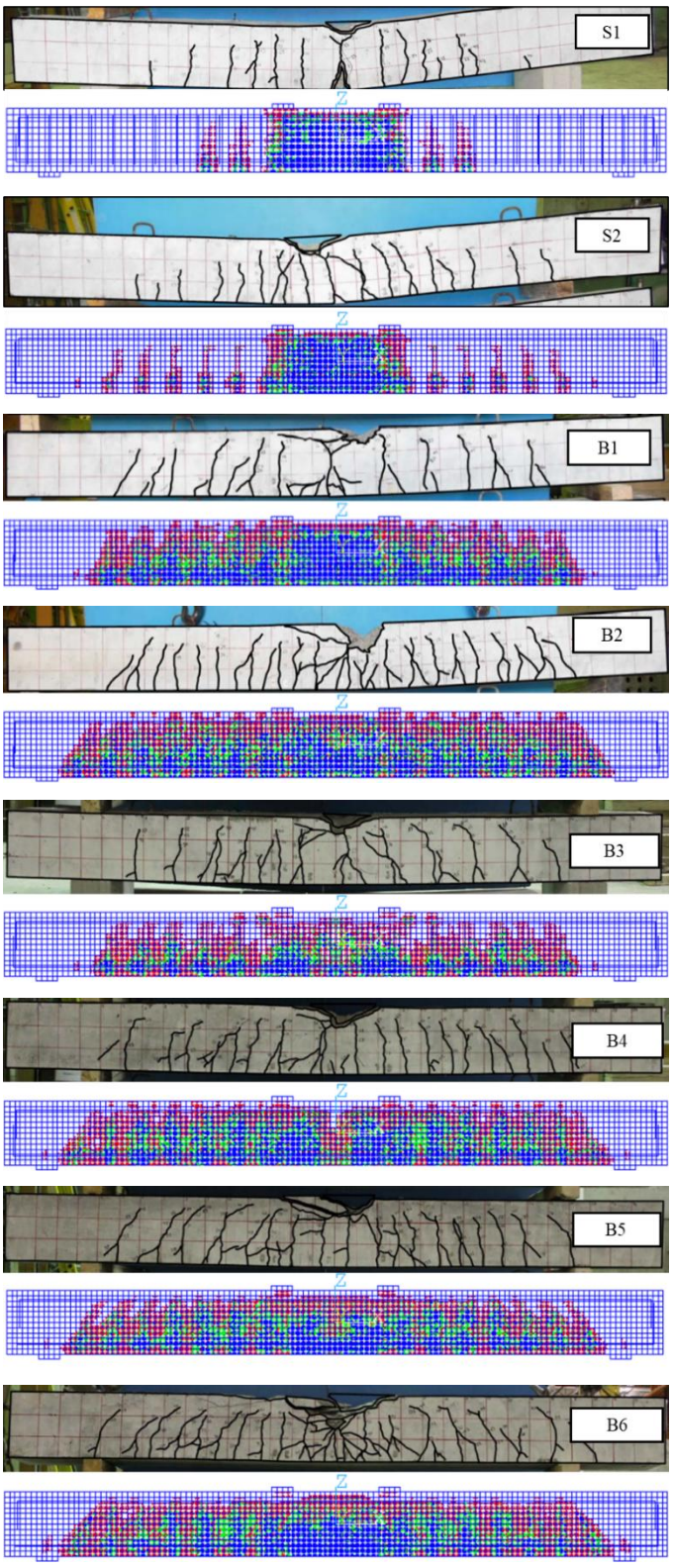

Figure 10. Crack pattern comparison of experiment by Elgabbas et al. [24] and FEM predictions

In the steel-reinforced specimens (S1 and S2), the FEM model demonstrated the expected ductile response, characterized by flexural cracks initiating at the tension face and eventual crushing of concrete in the compression zone at mid-span. By contrast, the BFRP-reinforced beams (B1–B6) exhibited more widely distributed cracking along the beam span, consistent with their linear-elastic behavior. Crack development followed a systematic sequence: initial flexural cracks formed at mid-span, then propagated toward the supports with further loading. As the load increased, vertical cracks widened and deepened, in line with trends reported in previous studies [24, 26, 34]. At advanced load stages, several vertical cracks near the supports evolved into diagonal cracks, with crack density and distribution strongly influenced by reinforcement ratio.

Stress distribution maps, shown through color coding, further confirmed these mechanisms: low tensile stresses were indicated in blue, intermediate stresses in green–yellow, and high stress concentrations in red. Both numerical and experimental results consistently demonstrated flexural cracking in regions of positive bending moment, supporting the reliability of the FEM predictions [48].

Figure 11 presents a direct comparison of experimental and FEM crack development in reinforced beams. The results highlight the fundamental progression of flexural behavior: cracks initiate at the tensile surface, propagate into the constant-moment region, and subsequently develop into diagonal cracks within the shear span, while concrete crushing dominates in the compression zone at ultimate load. Importantly, the FEM captured the concrete crushing mechanism without indicating premature shear failure near the supports, aligning well with experimental outcomes.

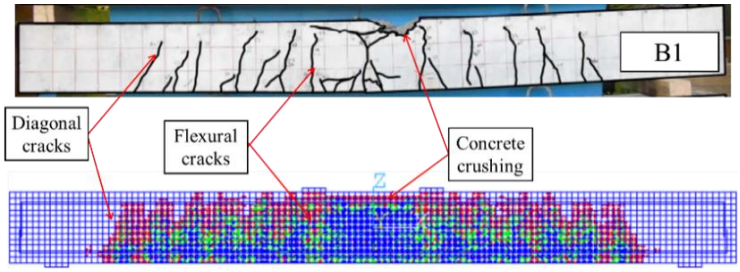

Figure 11. Crack formation mechanisms and failure pattern analysis

Overall, the strong correlation between numerical predictions and experimental results validates the ability of FEM to simulate crack initiation, propagation, and ultimate failure in reinforced beams. These findings are consistent with those of Abushanab et al. [35] and Godat et al. [46], who emphasized the importance of bond–slip and tension-stiffening effects in controlling crack formation. While FEM offers reliable prediction of crack behavior, refinement of bond–slip modeling would further enhance its ability to capture localized crack widths and spacing, particularly in BFRP-reinforced members.

4. Conclusions

This study investigated the flexural performance of basalt fiber-reinforced polymer (BFRP) and steel-reinforced concrete beams through finite element analysis (FEA), sectional analysis based on ACI 440.1R-15 and CSA S806-12 provisions, and experimental validation. Eight beam specimens, each with dimensions of 200 × 300 × 3,100 mm and tested under four-point bending with a clear span of 2,700 mm, were analyzed to evaluate ultimate moment capacity, moment–deflection behavior, and crack development. The principal findings are summarized as follows:

- The FEM model exhibited strong correlation with experimental results for steel-reinforced beams, with FEM-to-experimental ratios of 0.92 and 0.94 for specimens S1 and S2. For BFRP-reinforced beams, ratios ranged from 1.01 to 1.45, with FEM predictions generally overestimating capacities at higher reinforcement ratios. These outcomes confirm the accuracy of FEM for conventional reinforcement and its limitations for BFRP beams with large reinforcement ratios.
- BFRP-reinforced beams demonstrated higher ultimate moment capacities compared with steel-reinforced specimens. The moment–deflection relationships revealed consistent behavioral trends across experiments, FEM predictions, and design codes. Increasing the reinforcement ratio from 0.0029 to 0.0119 resulted in proportional enhancement of beam strength, although at the expense of ductility due to the brittle nature of BFRP reinforcement.
- Distinct failure modes were observed between reinforcement types. Steel-reinforced beams exhibited ductile behavior characterized by yielding and sustained resistance, whereas BFRP-reinforced beams failed in a brittle manner, with abrupt loss of capacity at peak load.
- FEM simulations implemented in ANSYS effectively predicted ultimate moment capacities, moment–deflection responses, and crack propagation patterns. This computational approach provides a cost-effective and reliable tool for evaluating BFRP-reinforced concrete beams, offering potential applications in design optimization and parametric studies where experimental testing may be limited.
- The systematic overestimation of capacity by FEM relative to experiments and design codes reflects inherent limitations in the adopted concrete material models, particularly under combined cracking and crushing with perfect bond assumptions. These modeling simplifications, also reported in previous studies [44–45, 47], emphasize the need for further refinement.

Overall, this research highlights the potential of FEM as a predictive tool for assessing the behavior of BFRP-reinforced beams, while also confirming the conservative and safety-oriented nature of ACI 440.1R-15 and CSA S806-12 provisions. Future research should incorporate bond–slip models, tension-stiffening effects, and nonlinear fracture mechanics into FEM simulations, as well as extend the framework to shear-dominated, dynamic, and hybrid reinforcement systems. These refinements will enhance predictive accuracy and provide more comprehensive guidance for the structural application of BFRP reinforcement, particularly in bridge decks and marine structures, where its durability against chloride and sulfate attack is especially advantageous.

5. Declarations

5.1. Author Contributions

Conceptualization, P.S., A.K., and S.T.; methodology, P.S., A.K., and S.T.; software, A.K.; validation, P.S., A.K., and S.T; formal analysis, P.S., A.K., and S.T.; investigation, P.S. and A.K.; resources, P.S. and A.K.; data curation, P.S. and S.T.; writing—original draft preparation, P.S. and S.T.; writing—review and editing, S.T., P.F., P.I., Y.S., W.K., C.T., and P.C.; visualization, S.T. and P.C.; supervision, S.T., P.F., P.I., Y.S., W.K., C.T., and P.C.; project administration, S.T.; funding acquisition, S.T. All authors have read and agreed to the published version of the manuscript.

5.2. Data Availability Statement

The data presented in this study are available on request from the corresponding author.

5.3. Funding and Acknowledgments

This research was financially supported by the Sustainable Infrastructure Research and Development Center, Department of Civil Engineering, Faculty of Engineering, Khon Kaen University, Khon Kaen, Thailand. The authors also gratefully acknowledge the financial and institutional support provided by the Research and Graduate Studies program of Khon Kaen University.

5.4. Conflicts of Interest

The authors declare no conflict of interest.

6. References

[1] Madotto, R., Van Engelen, N. C., Das, S., Russo, G., & Pauletta, M. (2021). Shear and flexural strengthening of RC beams using BFRP fabrics. Engineering Structures, 229. doi:10.1016/j.engstruct.2020.111606.

[2] Siddika, A., Mamun, M. A. Al, Alyousef, R., & Amran, Y. H. M. (2019). Strengthening of reinforced concrete beams by using fiber-reinforced polymer composites: A review. Journal of Building Engineering, 25. doi:10.1016/j.jobe.2019.100798.

[3] Sorrentino, L., Turchetta, S., & Bellini, C. (2017). In process monitoring of cutting temperature during the drilling of FRP laminate. Composite Structures, 168, 549–561. doi:10.1016/j.compstruct.2017.02.079.

[4] Ou, Y., & Zhu, D. (2015). Tensile behavior of glass fiber reinforced composite at different strain rates and temperatures. Construction and Building Materials, 96, 648–656. doi:10.1016/j.conbuildmat.2015.08.044.

[5] Naser, M. Z., Hawileh, R. A., & Abdalla, J. (2021). Modeling strategies of finite element simulation of reinforced concrete beams strengthened with FRP: A review. Journal of Composites Science, 5(1), 19. doi:10.3390/jcs5010019.

[6] Rajak, D., Pagar, D., Menezes, P., & Linul, E. (2019). Fiber-Reinforced Polymer Composites: Manufacturing, Properties, and Applications. Polymers, 11(10), 1667. doi:10.3390/polym11101667.

[7] Fan, X., Gu, S., Wu, X., & Jiang, J. (2020). Critical shear crack theory-based punching shear model for FRP-reinforced concrete slabs. Advances in Structural Engineering, 24(6), 1208–1220. doi:10.1177/1369433220978146.

[8] Abbood, I. S., Odaa, S. A., Hasan, K. F., & Jasim, M. A. (2021). Properties evaluation of fiber reinforced polymers and their constituent materials used in structures - A review. Materials Today: Proceedings, 43, 1003–1008. doi:10.1016/j.matpr.2020.07.636.

[9] Feng, X., Liu, D., Guo, Y., Zhong, F., Zuo, J., & Liu, W. (2024). Research on mechanical performance of longitudinal joints in segmental tunnel linings strengthened by fiber-reinforced plastic grid with polymer-cement-mortar method. Frontiers of Structural and Civil Engineering, 18(10), 1610–1625. doi:10.1007/s11709-024-1105-z.

[10] Qiong, T., Jha, I., Bahrami, A., Isleem, H. F., Kumar, R., & Samui, P. (2024). Proposed numerical and machine learning models for fiber-reinforced polymer concrete-steel hollow and solid elliptical columns. Frontiers of Structural and Civil Engineering, 18(8), 1169–1194. doi:10.1007/s11709-024-1083-1.

[11] ACI 440.1R-15. (2015). Guide for the Design and Construction of Concrete Reinforced with FRP Bars. American Concrete Institute (ACI), Farmington Hills, United States.

[12] CAN/CSA S806-12. (2012). Design and Construction of Building Components with Fibre Reinforced Polymers. Canadian Standard Association (CSA), Toronto, Canada.

[13] Sirimontree, S., Keawsawasvong, S., & Thongchom, C. (2021). Flexural behavior of concrete beam reinforced with GFRP bars compared to concrete beam reinforced with conventional steel reinforcements. Journal of Applied Science and Engineering, 24(6), 883–890. doi:10.6180/jase.202112_24(6).0009.

[14] Sivasankar, S., Dhal, L., Gopalakrishnan, R., Velrajkumar, G., & Jose, A. (2023). Strength and ductility of reinforced concrete using basalt fibre-reinforced polymers. Polymer Bulletin, 81(7), 6473–6493. doi:10.1007/s00289-023-05010-1.

[15] Deng, J., Liu, A., Ma, Z. J., Huang, P., & Zhou, R. (2015). Interfacial Behavior of RC Beams Strengthened with FRP under Fatigue Loading. Advances in Structural Engineering, 18(2), 283–293. doi:10.1260/1369-4332.18.2.283.

[16] He, J., Lei, D., She, Z., & Xi, B. (2023). Investigation on bonding behavior of basalt fiber reinforced polymer (BFRP) sheet reinforced concrete beam. Journal of Building Engineering, 75. doi:10.1016/j.jobe.2023.106963.

[17] Ibrahim, A. M., & Fawzy, M. S. (2023). Strengthening of RC flat slabs against punching shear with GFRP laminates adopting a hybrid technique. Engineering and Applied Science Research, 50(5), 490–498. doi:10.14456/easr.2023.51.

[18] Monaldo, E., Nerilli, F., & Vairo, G. (2019). Basalt-based fiber-reinforced materials and structural applications in civil engineering. Composite Structures, 214, 246–263. doi:10.1016/j.compstruct.2019.02.002.

[19] Liu, K., Wulan, T., Yao, Y., Bian, M., & Bao, Y. (2024). Assessment of damage evolution of concrete beams strengthened with BFRP sheets with acoustic emission and unsupervised machine learning. Engineering Structures, 300. doi:10.1016/j.engstruct.2023.117228.

[20] Al-Hamrani, A., & Alnahhal, W. (2023). Bond durability of sand coated and ribbed basalt FRP bars embedded in high-strength concrete. Construction and Building Materials, 406. doi:10.1016/j.conbuildmat.2023.133385.

[21] Yeboah, D., Taylor, S., McPolin, D., & Gilfillan, R. (2013). Pull-out behaviour of axially loaded Basalt Fibre Reinforced Polymer (BFRP) rods bonded perpendicular to the grain of glulam elements. Construction and Building Materials, 38, 962–969. doi:10.1016/j.conbuildmat.2012.09.014.

[22] Attia, K., Alnahhal, W., Elrefai, A., & Rihan, Y. (2019). Flexural behavior of basalt fiber-reinforced concrete slab strips reinforced with BFRP and GFRP bars. Composite Structures, 211, 1–12. doi:10.1016/j.compstruct.2018.12.016.

[23] Zheng, Y., Zhang, Y., Zhuo, J., Zhang, Y., & Wan, C. (2022). A review of the mechanical properties and durability of basalt fiber-reinforced concrete. Construction and Building Materials, 359, 129360. doi:10.1016/j.conbuildmat.2022.129360.

[24] Elgabbas, F., Ahmed, E. A., & Benmokrane, B. (2017). Flexural Behavior of Concrete Beams Reinforced with Ribbed Basalt-FRP Bars under Static Loads. Journal of Composites for Construction, 21(3). doi:10.1061/(asce)cc.1943-5614.0000752.

[25] High, C., Seliem, H. M., El-Safty, A., & Rizkalla, S. H. (2015). Use of basalt fibers for concrete structures. Construction and Building Materials, 96, 37–46. doi:10.1016/j.conbuildmat.2015.07.138.

[26] El Refai, A., Alnahhal, W., Al-Hamrani, A., & Hamed, S. (2022). Shear performance of basalt fiber-reinforced concrete beams reinforced with BFRP bars. Composite Structures, 288. doi:10.1016/j.compstruct.2022.115443.

[27] Yang, Y., Fang, S., Feng, W., Wan, S., Li, L., & Tang, Y. (2023). Flexural and compressive performance of BFRP-reinforced geopolymer sea-sand concrete beams and columns: Experimental and analytical investigation. Composite Structures, 318. doi:10.1016/j.compstruct.2023.117089.

[28] Sun, W., Zheng, Y., Zhou, L., Song, J., & Bai, Y. (2020). A study of the bond behavior of FRP bars in MPC seawater concrete. Advances in Structural Engineering, 24(6), 1110–1123. doi:10.1177/1369433220956816.

[29] Yuan, F., Liu, P., Li, H., & Wu, Y. (2024). Experimental investigations on the flexural behavior of compression-cast seawater sea-sand concrete beams reinforced with CFRP bars. Construction and Building Materials, 445. doi:10.1016/j.conbuildmat.2024.137754.

[30] Ovitigala, T., Ibrahim, M. A., & Issa, M. A. (2016). Serviceability and Ultimate Load Behavior of Concrete Beams Reinforced with Basalt Fiber-Reinforced Polymer Bars. ACI Structural Journal, 113(4). doi:10.14359/51688752.

[31] Attia, K., El Refai, A., & Alnahhal, W. (2020). Flexural behavior of basalt fiber–reinforced concrete slab strips with BFRP bars: Experimental testing and numerical simulation. Journal of Composites for Construction, 24(2). doi:10.1061/(ASCE)CC.1943-5614.0001002.

[32] Grzesiak, S., Schultz-Cornelius, M., & Pahn, M. (2023). Experimental and analytical evaluation of externally bonded BFRP and CFRP strips on the load-bearing behaviour of reinforced concrete structures using distributed fibre optic sensing. Construction and Building Materials, 400. doi:10.1016/j.conbuildmat.2023.132452.

[33] Muhammad, J. H., & Yousif, A. R. (2023). Effect of basalt minibars on the shear strength of BFRP-reinforced high-strength concrete beams. Case Studies in Construction Materials, 18. doi:10.1016/j.cscm.2023.e02020.

[34] Van Hong Bui, L., Thongchom, C., Sirimontree, S., Nguyen, P. T., Nguyen, T.-T., Keawsawasvong, S., Nuaklong, P., & Jongvivatsakul, P. (2022). Experimental, numerical, and analytical study of concrete beams reinforced with steel stirrups and embedded with functional plates. Structures, 39, 293–309. doi:10.1016/j.istruc.2022.03.013.

[35] Abushanab, A., Alnahhal, W., & Farraj, M. (2022). Experimental and finite element studies on the structural behavior of BFRC continuous beams reinforced with BFRP bars. Composite Structures, 281. doi:10.1016/j.compstruct.2021.114982.

[36] Zidani, M. B., Belakhdar, K., Tounsi, A., & Adda Bedia, E. A. (2015). Finite element analysis of initially damaged beams repaired with FRP plates. Composite Structures, 134, 429–439. doi:10.1016/j.compstruct.2015.07.124.

[37] Hawileh, R. A., Assad, M. A., Abdalla, J. A., & Naser, M. Z. (2024). Finite element modeling of reinforced concrete beams externally bonded with PET-FRP laminates. Computers and Concrete, 33(2), 163–173. doi:10.12989/cac.2024.33.2.163.

[38] Tran, H., Nguyen-Thoi, T., & Dinh, H. B. (2025). State-of-the-Art Review of Studies on the Flexural Behavior and Design of FRP-Reinforced Concrete Beams. Materials, 18(14), 3295. doi:10.3390/ma18143295.

[39] Kazemi, M., Madandoust, R., Chastre, C., Reza Esfahani, M., & Courard, L. (2021). Numerical study on the flexural behaviour of normal- and high-strength concrete beams reinforced with GFRP bar, using different amounts of transverse reinforcement. Structures, 34, 3113–3124. doi:10.1016/j.istruc.2021.09.077.

[40] Badawi, M. I., Badawi, M. I., & Awwad, M. (2025). Investigation of an Innovative Technique for R.C. Square Footing Reinforced by GFRP and BFRP Bars with HSC. Civil Engineering Journal (Iran), 11(4), 1547–1562. doi:10.28991/CEJ-2025-011-04-017.

[41] Willam, K. J., & Warnke, E. P. (1975). Constitutive model for the triaxial behavior of concrete. IABSE Proceedings, 19, 1–30.

[42] Dahmani, L., Khennane, A., & Kaci, S. (2010). Crack identification in reinforced concrete beams using ANSYS software. Strength of Materials, 42(2), 232–240. doi:10.1007/s11223-010-9212-6.

[43] Hognestad, E., Hanson, N. W., & McHenry, D. (1961). Rectangular Concrete Stress Distribution in Ultimate Strength Design. ACI Journal Proceedings, 52(12), 11609. doi:10.14359/11609.

[44] Vacev, T., Bonić, Z., Prolović, V., Davidović, N., & Lukić, D. (2015). Testing and finite element analysis of reinforced concrete column footings failing by punching shear. Engineering Structures, 92, 1–14. doi:10.1016/j.engstruct.2015.02.027.

[45] Mohyeddin, A., Goldsworthy, H. M., & Gad, E. F. (2013). FE modelling of RC frames with masonry infill panels under in-plane and out-of-plane loading. Engineering Structures, 51, 73–87. doi:10.1016/j.engstruct.2013.01.012.

[46] Godat, A., Chaallal, O., & Obaidat, Y. (2020). Non-linear finite-element investigation of the parameters affecting externally-bonded FRP flexural-strengthened RC beams. Results in Engineering, 8. doi:10.1016/j.rineng.2020.100168.

[47] Ahmed, H. Q., Jaf, D. K., & Yaseen, S. A. (2020). Flexural strength and failure of geopolymer concrete beams reinforced with carbon fibre-reinforced polymer bars. Construction and Building Materials, 231, 117185. doi:10.1016/j.conbuildmat.2019.117185.

[48] Abdel-Jaber, M., Al-Nsour, R., & Ashteyat, A. (2025). Flexural strengthening and rehabilitation of continuous reinforced concrete beams using BFRP sheets: Experimental and analytical techniques. Composites Part C: Open Access, 16. doi:10.1016/j.jcomc.2024.100556.